An improved geometric lunar figure from *Chang'E-1* and *SELENE* laser altimetry

H. Bâki Iz, C. K. Shum, Y. Q. Chen and C. L. Dai

Abstract. This study calibrates the footprint positions of 8.5 million *Chang'E-1* and 8.8 million *SELENE* laser altimetry measurements against accurately known lunar laser reflector locations. The resulting datasets are used to estimate triaxial, biaxial and spherical models of the lunar figure based on the two datasets individually. The equatorial semi-major, minor and polar axes of the *Chang'E-1* and *SELENE* solutions differ by −143 m, 3 m and −49 m respectively. The differences between their geometric centers and the lunar center of mass along the three axes are 186 m, 3 m, and 52 m. The complete laser altimetry datasets from the two missions reveal a lunar figure that is more spherical than previously thought. Furthermore, the *Chang'E-1* and *SELENE* solutions are in better agreement with each other than either is with the ULCN 2005 lunar figure.

Keywords. Lunar figure, Chang'E-1, SELENE, ULCN 2005, Laser Altimetry.

Introduction

The recent *Chang'E-1* (China) and *SELENE* (Japan) missions have produced over 17 million laser altimetry measurements (averaging approximately 1 measurement for every 2 square km of coverage) of the lunar surface. The parameters of the lunar figure are of interest to lunar exploration, and can be derived from these measurements. Furthermore, improved quantification of the geometric and dynamic lunar figure allows one to study the origin, interior structure, and composition of the moon. Finally, horizontal lunar control networks supporting lunar mapping (as in the case of GPS on Earth) require a precise mathematical reference surface. To support the above goals, this study presents new estimates of the best fitting triaxial ellipsoid, biaxial (rotational) ellipsoid, and sphere, along with their geometric centers (with respect to the center of mass of the moon). These models are derived from the largest datasets of *Chang'E-1* and *SELENE* laser altimetry measurements to date.

Recent approaches to modeling lunar topography use a spherical harmonic representation. For example, Bills and Ferrari (1977) calculated the parame-

ters of a triaxial ellipsoid from spherical harmonics up to degree 12 fit to Earth-based and orbital observations. More recently, Smith et al. (1997) produced a Goddard Lunar Topography Model (GLTM 2) composed of spherical harmonics up to degree and order 72, based on the mass-centered radii deduced from *Clementine* laser altimetry measurements.

Other techniques for determining the lunar figure involve data from spaceborne missions such as the Lunar Orbiter. These data are corrected for the position of the spacecraft at the time of exposure using photogrammetric techniques (Ruben 1969), and an important part of this process is calculating the positions of prominent lunar features that appear on the pictures. The recent Unified Lunar Control (ULCN 2005) model is a fusion of photogrammetrically determined 2D control points (ULCN 1994) and *Clementine* Lunar Control Networks (CLCN), which also include laser altimetry. In a recent study, Iz (2009) estimated parameters for selenocentric and non-selenocentric triaxial ellipsoids, rotation ellipsoids, and spheres from lunar control points generated by the ULCN 2005 solution, expressed in selenocentric coordinates (latitude, longitude and selenocentric distance). His analysis does not use harmonic models of the lunar topography. The present study follows the same geometric approach to modeling the lunar figure, but uses the footprint positions of 8.5 million *Chang'E-1* and 8.8 million *SELENE* lunar laser altimetry measurements which have been recently released to the scientific community.

Data sources

A laser altimeter on board a spacecraft transmits a high-power, narrow laser pulse to the surface and receives the reflected photons using an optical telescope. The distance between the satellite and the surface is determined by measuring the time delay of the laser pulses. The center of mass of the Moon can be calculated from the precise spacecraft orbits. Thus, the height of the lunar surface can be determined by subtracting the laser altimetry measurement from the distance between the spacecraft and the center of mass of the Moon. This number is the selenocentric radial distance. The 3D location of the

measurement is also specified using the latitude and longitude of the subsatellite point on the surface of the Moon (usually in the body-fixed, mean Earth/polar axis reference system).

Chang'E-1, launched on 24 October 2007, is China's first lunar exploration mission. It is a single satellite in a two-hour polar orbit, with an inclination of $90° \pm 2°$ and an altitude of 200 km. The onboard laser altimetry system produced measurements with a 120 m footprint at 200 km satellite altitude. The precision of the laser altimetry measurements is estimated to be better than 5 m (Ping et al. 2009). The along-track footprint spacing was about 1.4 km. After two months of data acquisition, the minimum footprint spacing along the equator was about 7.5 km. In this study, over 8.5 million selenocentric distances (after removing over 300,000 outliers) are used to determine the lunar figure parameters, along with their corresponding latitudes and longitudes provided by the China Lunar Exploration Center.

The *SELENE* mission launched on 14 September 2007. *KAGUYA*, the main satellite, occupies a one-hour polar orbit with an inclination of 90 ± 1 degrees at an altitude of 100 ± 30 km. Its onboard laser altimetry system produced measurements with a footprint of 40 m and a spacing of about 1.6 km along the track. The precision of its laser altimetry range measurements is also 5 m (Araki et al. 2009). JAXA (2009) provided over 8.8 million selenocentric laser altimetry measurements based on these data, along with subsatellite locations (latitudes and longitudes), precise orbits, and other mission parameters.

The lunar figure parameters derived by Iz (2009) from the ULCN 2005 control points are also used for comparison. The ULCN control network consists of 272,931 points with an average surface density of approximately one per 46 km^2 (Archinal et al. 2006). The precision of the ULCN 2005 control points is reported to be a few hundred meters (Iz et al. 2009).

All data sets are referenced to a spherical coordinate system whose polar axis is the mean Earth/Moon axis and whose center is the Moon's center of mass. All laser altimetry measurements (*Chang'E-1* and *SELENE*) and station positions (ULCN 2005) are expressed in this reference frame.

Calibration of the laser altimetry footprint radial distances

The footprint coordinates calculated from *Chang'E-1* and *SELENE* laser altimetry are subject to random and systematic errors. The latter can be determined by calibrating the data to the accurately known radial coordinates of nearby Lunar Laser Ranging Retroreflector (LLRR) sites (Apollo 11, 14, 15, and Lunakhod 2) and radio-tracked Apollo Lunar Surface Experiments Package (ALSEP) sites (Apollo 12, 14, 15, 16, and 17). The locations of these sites are marked in Figure 1. Some ALSEP sites are not included in the calibration because they are very close to the more precisely measured LLRR sites (within 42 m).

The largest errors to consider are orbital in nature, caused by errors in the lunar gravity field model
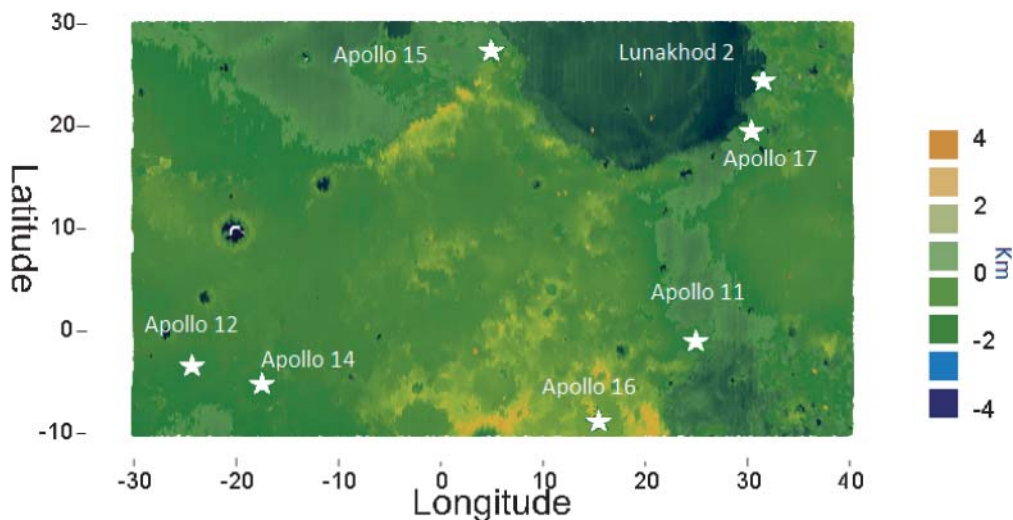

Figure 1: The locations of LLRRs and ALSEPs on the Moon.

and errors or gaps in satellite tracking. These errors are especially important for *Chang'E-1*. Unlike *SELENE*, *Chang'E-1* did not have a relay satellite providing tracking over the far side of the Moon. Orbital errors propagate directly into the laser altimetry through the radial, along-track and cross-track components of the satellite's footprint positions (Ping et al. 2009, Goossens et al. 2009). A constant radial orbit error translates into a scale error in the lunar shape parameters. Horizontal errors in the footprint positions, on the other hand, mainly affect the position of the geometric center of the lunar figure with respect to the lunar center of mass. Among the three orbital error components, radial errors are usually smaller in magnitude and easier to calibrate from accurate laser altimetry measurements, the well-observed radial components of LLRR sites (Davies and Colvin 2000), and ALSEP locations (King et al. 1976). Systematic errors in the horizontal footprint positions are larger and more difficult to model, since there are no footprints colocated with LLRR and ALSEP sites despite the dense coverage of the *Chang'E-1* and *SELENE* laser altimetry measurements. However, because systematic along-track and cross-track errors are normal to the radial errors, they do not affect the lunar shape parameters significantly but only contaminate estimates of the center of the figure. Therefore, in the absence of other information, this study only calibrates the systematic radial errors.

The radial precisions of the satellite orbits have been quantified through analysis of laser altimetry measurements separated in time at the same geographic location, comparing ascending and descending ground tracks of the satellite. The radial orbit errors are reported to be 30 m for *Chang'E-1* (Ping et al. 2009), and just 1 m for *SELENE* (Goossens et al. 2009).

The laser altimetry errors of *Chang'E-1* and *SELENE* are small compared to their respective orbital errors of ± 5 and ± 1 m (Ping et al. 2009, Goossens et al. 2009). One remaining concern about systematic range errors is the distortion of return pulses by the target terrain, which may be sloped or rough and has an unknown albedo (Gardner 1992). This source of uncertainty introduces an additional range error of approximately ± 12 m (Araki et al. 2009b).

Despite their somewhat larger uncertainties of ± 30 m in the radial coordinate and ± 10 m in the horizontal (King et al. 1976), ALSEP locations still contribute meaningfully to the calibration and are included in our analysis. The LLRR locations,

which are accurate to ± 1 m radially (Davies and Colvin 2000), are also included.

A large error specific to our calibration approach arises because none of the laser altimetry pulses is located near the LLRR and ALSEP sites. Hence, the radial distances of hypothetical laser footprints at the LLRR and ALSEP locations need to be interpolated from digital elevation models constructed using nearby footprint positions. Since both satellites are in polar orbits, the footprints are spaced regularly and frequently only along the North-South direction. Their distribution in the East-West direction is not suitable for creating digital terrain models. Moreover, currently unknown reference frame differences render the identification of the nearby footprints ambiguous, unless aided by satellite imagery. It is therefore more appropriate to interpolate from a large number of nearby footprint locations and introduce a radial *proximity error*. This random error is defined as the error caused by using nearby points as if they are collocated. The error is assumed to be proportional to the distance to nearby LLRR or ALSEP locations. The coefficient of the proximity error is chosen conservatively at ± 10 m per km, which introduces a maximum uncertainty of ± 100 m for a footprint 10 km away from a LLRR or ALSEP site. By far, this is the largest radial error source, but it is unavoidable in order to represent the error conservatively.

In light of the aforementioned error sources, the stochastic calibration model reads as

$$\mathbf{r}_{LAL} - \mathbf{r}_{REF} = \Delta + \boldsymbol{\varepsilon}_T, \quad \boldsymbol{\varepsilon}_\mathbf{T} \sim (0, \sigma_T^2 \mathbf{I}_{n\times 1}), \quad (1)$$

where $\mathbf{r}_{LAL}$ and $\mathbf{r}_{REF}$ are $n \times 1$ vectors containing the radial distances of the LLRR and ALSEP locations and the n laser altimetry measurements respectively. The unknown parameter Δ represents any unmodeled, constant systematic errors common to all measurements at the calibration locations. $\boldsymbol{\varepsilon}_T$ is the $n \times 1$ random error in the differences $\mathbf{r}_{LAL} - \mathbf{r}_{REF}$. Its components are assumed to be statistically independent. The diagonal elements σ_T^2 of the covariance matrix are the sum of squares of various error sources. Assuming the errors are additive and independent of each other, the total error is the sum of squares of the various errors (SSE):

$$\sigma_T^2 := \sigma_{REF}^2 + \sigma_{RadialOrbit}^2 + \sigma_{Ranging}^2$$
$$+ \sigma_{RangeShift}^2 + \sigma_{Proximity}^2 \quad (2)$$

The magnitudes of these errors are summarized in Table 1.

Table 1: Error sources and estimated calibration constants for the radial distances of *Chang'E-1* and *SELENE* footprints. Only laser altimetry measurements within 10 km of the LLRR and ALSEP locations are considered in the calibration. The total number of such footprints, listed within parentheses, was reduced by removing outliers. All units are in meters.

Error	Chang'E-1	SELENE
LLRR radial error	1	1
ALSEP radial error	30	30
Radial orbit error	30	1
Proximity error	$10 \times d$ (km)	$10 \times d$ (km)
Laser altimetry ranging error	5	1
Laser altimetry range shift error	12	12
Total no. of data	251(299)	288(338)
Estimated calibration constant	-116 ± 4	-4 ± 4

As an example, Figure 2 shows the distribution of *Chang'E-1* and *SELENE* laser altimetry measurements within 10 km of the Lunakhod 2 LLRR site. The same criterion (altimetry data within 10 km) is applied to all the other calibration sites, resulting in a total of 299 and 338 laser altimetry measurements from the *Chang'E-1* and *SELENE* missions respectively. Figure 3 plots the differences between footprint radius and calibration site radius for the entire sample. This analysis reveals some significant outliers, mainly at the Lunakhod 2 (LLRR) and ALSEP 17 stations (both stations lie along the rough rim of *Mare Serenitatis*).

The least squares solution to Equation (1) is equivalent to a weighted mean of the differences between LLRR and ALSEP radial distances and nearby footprint radial distances. First, an initial weighted least squares solution is derived using Equation 2. Any radial differences with residuals exceeding 200 m (approximately 6 times the dominant radial error) were then removed from the calibration data. The remaining sample includes 251 and 288 radial differences for the *Chang'E-1* and *SELENE* satellites respectively. Second, the calibration constants were estimated again using weights equal to the inverse squares of the residuals calculated after the initial solution. This method gives a more realistic assessment of the weights.

Figure 4 shows the distribution of residuals for the radial distance differences, along with their one sigma error bars. The residuals within each location are not randomly distributed, especially for the *Chang'E-1* data. The patterns can be attributed to an incomplete model of the terrain and satellite pass

biases. Fortuitously, there are no large-scale, systematic trends in the residuals for either mission, so the differences in radial coordinates can still be characterized as a random error.

The estimated calibration constant for the *Chang'E-1* data is large and statistically significant (-116 ± 4 m). The calibration constant for the *SELENE* data is -4 ± 4 m, consistent with zero. Hence, subsequent computations will use corrected *Chang'E-1* radial components (*adding* 116 m) but the original *SELENE* data.

It is important to note that these calibrations are local in nature and limited by the distribution of LLRR and ALSEP locations, which are only available on the near side of the moon.

Estimation of lunar figure parameters

Three variants of the lunar figure were considered: a triaxial ellipsoid, a biaxial ellipsoid, and a sphere. The triaxial ellipsoid is characterized by an equatorial semi-major axis *a*, a semi-minor axis *b*, and a polar axis *c*. The three axes are oriented towards the Earth, in the plane of the sky perpendicular to the polar axis, and along the polar axis respectively. The three axes are *unknown parameters*. In the equation below, the Cartesian coordinates *x*, *y*, *z*, refer to the locations of the footprints. The center of the figure, x_c, y_c, z_c, is also unknown. All Cartesian coordinates are measured with respect to the underlying mean Earth/polar axis reference frame centered on the center of mass of the Moon,

$$\frac{(x - x_c)^2}{a^2} + \frac{(y - y_c)^2}{b^2} + \frac{(z - z_c)^2}{c^2} - 1 = 0 \quad (3)$$

The second model is a special case of (3), with equatorial semi-major and minor axes $a = b$, representing a rotational ellipsoid. No *a priori* constraints ensure that $a > c$; hence, the model can represent an *oblate* or *prolate* ellipsoid. The third model is a sphere with radius $a = b = c = R$.

A uniformly weighted iterative algorithm (Pope 1972) is used in a partitioned computational scheme (Iz 2009) to estimate Equation (3) given the suitably calibrated and weighted footprint coordinates. To determine the relative weights of the *Chang'E-1* and *SELENE* data, we assume Cartesian coordinate errors of 30 and 12 m respectively, equivalent to the largest source of random error in the radial coordinate. These values are derived from the footprint radial error σ^2:
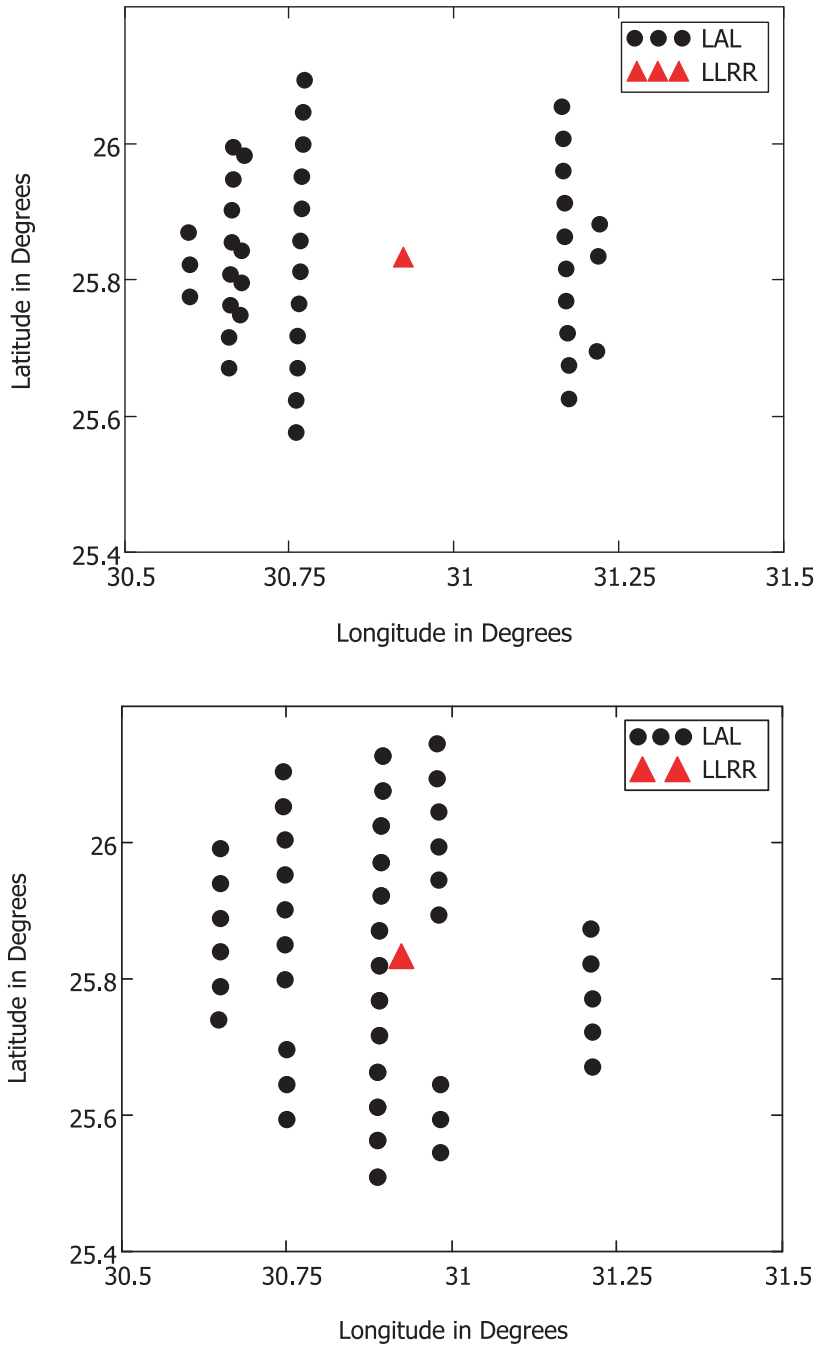
Figure 2: The locations of *Chang'E-1* (top), and *SELENE* (bottom) laser altimetry footprints within 10 km of the Lunakhod 2 LLRR site. One degree corresponds to approximately 30 km on the surface of the moon.

$$\sigma^2 := \sigma^2_{RadialOrbit} + \sigma^2_{Ranging}$$
$$+ \sigma^2_{RangeShift} + \sigma^2_{Calibration}, \tag{4}$$

with an *a priori* variance of unit weight equal to one. Note that the standard errors of the estimates need to be scaled by the a posteriori variance of unit weight, although the estimates are independent of the uniform weights. Note that because the residuals shown in Figure 4 are influenced by real lunar topography, the calibration step is more important than the random error for realistic estimates of the lunar figure.
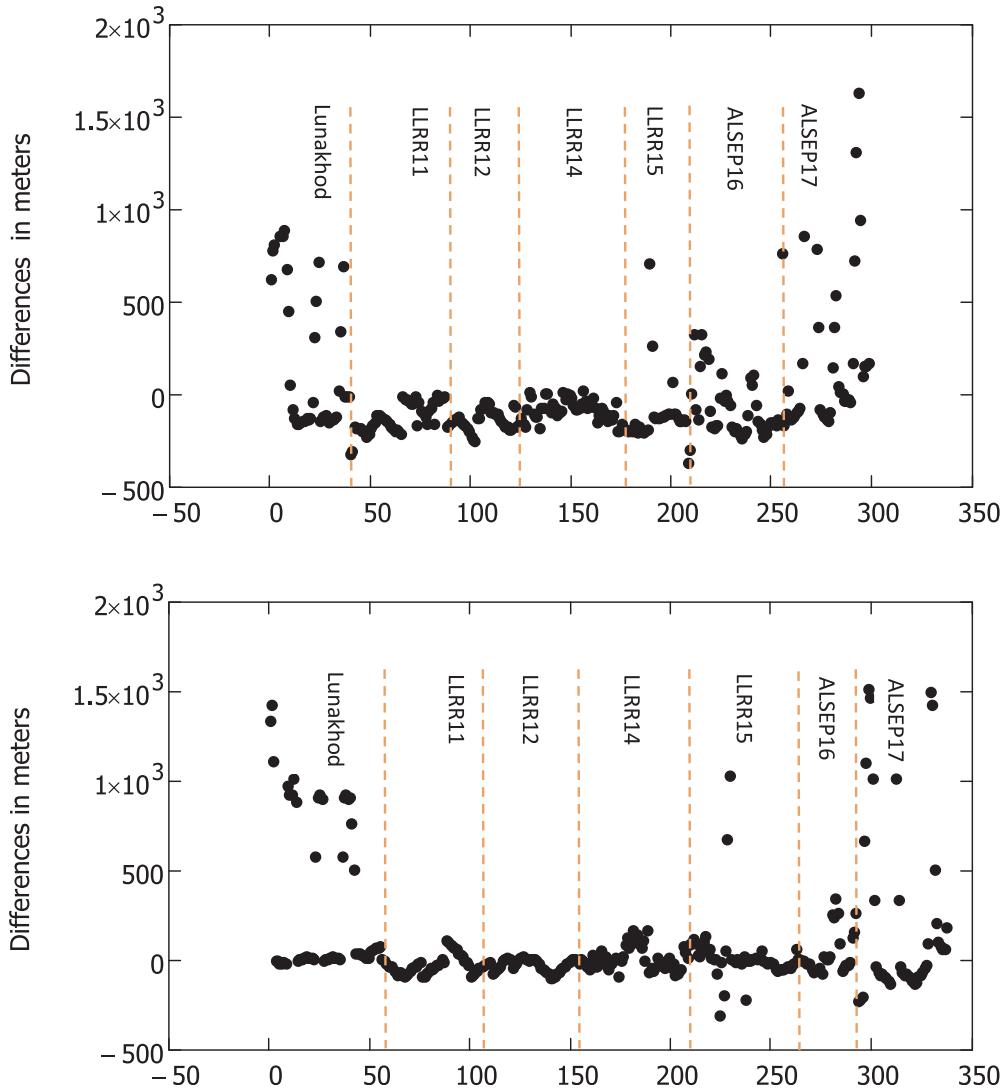
Figure 3: The radial differences between reference sites and laser altimetry footprint locations for *Chang'E-1* (top) and SE-LENE (bottom). Only footprints within 10 km of a LLRR or ALSEP site are plotted. The horizontal axis refers to the index number of the difference, grouping measurements associated with the same reference site.

Table 2 lists the estimated parameters of the non-selenocentric lunar figures and their geometric centers with respect to the center of mass of the Moon, using just one of the available datasets: *Chang'E-1*, *SELENE* or ULCN 2005. The equatorial semi-minor axis estimates from the *Chang'E-1* and *SE-LENE* datasets agree to within 3 m, validating the quality of their calibrations. Had the *Chang'E-1* data not been calibrated, the differences between all shape parameters of the two solutions would have been much larger.

The equatorial semi-major, minor, and polar axes of the *Chang'E-1* and *SELENE* solutions differ by −143 m, 3 m and −49 m respectively. The differences in the geometric centers of these two models are 186 m, 3 m, and 52 m for the x_c, y_c, and z_c components respectively. Note that along the x and z directions, the differences in geometric center positions and axis lengths are similar in magnitude but have opposite signs. This can be explained by systematic distortions in the footprint coordinates (analogous to reference frame distortions), under certain assumptions to be explained below.

The systematic differences in Cartesian footprint positions from two different data sets, x, y, z and u, v, w, can be expressed as follows:
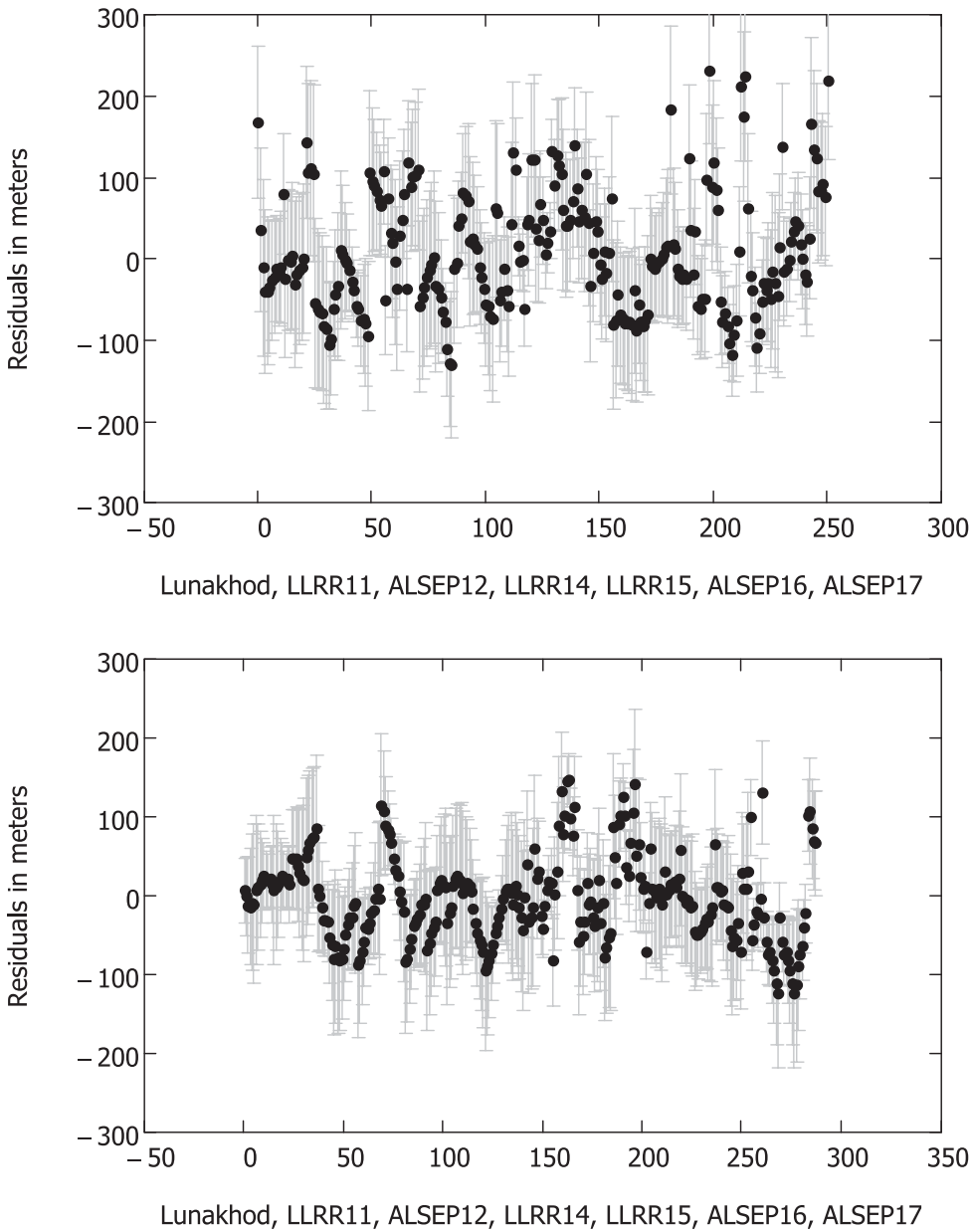
Figure 4: The residuals of topographical models in the vicinity of LLRRs and ALSEPs based on *Chang'E-1* (top), and SE-LENE (bottom) laser altimetry. Positions with residuals more than 200 m in magnitude in a preliminary model were removed from the dataset as outliers. Each residual is superimposed with its one-sigma error. The horizontal axis refers to the sequence of residuals.

$$u = u_0 + y\omega_{xy} + z\omega_{xz} + xe_{xx} + ye_{xy} + ze_{xz}$$

$$v = v_0 - x\omega_{xy} + z\omega_{yz} + ye_{yy} + xe_{xy} + ze_{yz} \quad (5)$$

$$w = w_0 - x\omega_{xz} - y\omega_{yz} + ze_{zz} + xe_{xz} + ye_{yz}$$

where, u_0, v_0, w_0 represent the translational shift between the two data sets. The rigid body rotations are denoted ω_{xy}, ω_{xz}, ω_{yz}. The linear strain parameters

involving compression or dilatation are denoted e_{xx}, e_{yy}, e_{zz}. The linear shear parameters for small deformations with respect to unity are denoted e_{xy}, e_{xz}, e_{yz}.

If there are only small translations and strains between the data sets (i.e., ω_{xy}, ω_{xz}, ω_{yz} *and* e_{xy}, e_{xz}, e_{yz} *all vanish) then two of the equations (5) can be*

Table 2: All units are meters. The equatorial semi-major and minor axes are denoted *a* and *b* respectively, and *c* is the polar axis. The location of the geometric center of the model in the mean Earth/polar axis reference system is given by x_c y_c z_c. The first set of parameters for each model is calculated using *Chang'E-1* data. The second set of parameters is derived from *SELENE* data, and the third set of parameters was obtained from the ULCN 2005 data (Iz 2009). All standard errors of the estimated parameters are less than a meter, except for the values within parentheses. N/A: Not applicable.

Model	a	b	c	x_c	y_c	z_c	d_c*	RMS**
Triaxial	1737810	1737597	1735947	−1485	−695	269	1662	1957
Ellipsoid	1737953	1737594	1735996	−1671	−698	207	1823	1885
	1737899(9)	1737570(9)	1735742(7)	−1658(6)	−681(6)	133(5)	1797	1754
Biaxial	1737708	N/A	1735946	−1485	−695	269	1662	1958
Ellipsoid	1737776		1735996	−1671	−699	207	1823	1887
	1737737(5)		1735741(7)	−1653(6)	−682(6)	133(5)	1793	1756
Sphere	1736797	N/A	N/A	−1491	−676	257	1657	2054
	1736905			−1682	−700	154	1828	1990
	1736965(6)			−1645(6)	−696(7)	142(6)	1792	1868

*d_c, distance between the center of the figure and the center of mass. **of residuals.

written as

$$u = u_0 + xe_{xx}$$
$$w = w_0 + ze_{zz} \quad (6)$$

The coordinate *v* is not included because distortions in this direction are negligible, as implied by the 3 m difference in the equatorial semi-minor axes of the *Chang'E-1* and *SELENE* solutions. If we assimilate *u* and *w* into the translation parameters and assume that their signs do not change, we obtain

$$\tilde{u}_0 \cong -xe_{xx}$$
$$\tilde{w}_0 \cong -ze_{zz} \quad (7)$$

The terms on the left-hand side of (7) are the differences in the *x* and *z* directions of the geometric centers. The terms on the right-hand side are scaled coordinates along the *x* and *z* axes, parallel to the equatorial semimajor axis *a* and polar axis *c* respectively. Therefore, these relationships explain the similarities in magnitude and opposite signs of the shape parameters and geometric center coordinates of the two models. It is likely that these differences are caused by unmodeled systematic effects in the *Chang'E-1* or *SELENE* orbits over the far side and polar regions, which could not be eliminated by our calibration of near-side data.

The origin of the *Chang'E-1* triaxial ellipsoid is closest to the lunar center of mass (refer to the distances d_c listed in Table 2). The choice of model (triaxial, biaxial, or spherical) has little effect on the accuracy of the figure center. Despite their differences, the *Chang'E-1* and *SELENE* solutions agree better with each other in several aspects of the lunar figure than

either model with the ULCN 2005 solution. For example, the polar flattening estimates of the three models are 1/986, 1/976 and, 1/871 for the *Chang'E-1*, *SELENE*, and ULCN 2005 biaxial solutions respectively. The geometric flattenings also reveal that the lunar shape is more spherical than the ULCN 2005 solution implies.

The standard errors are less than 1 m for all the *Chang'E-1* and *SELENE* estimates. This improvement in precision compared to the ULCN 2005 solution is mostly due to a 30-fold increase in the number of constraints *r*. The large number of measurements reduces the standard errors by a factor of approximately six, in proportion to the square root of *r*.

On the other hand, smaller standard errors are not indicative of a solution's accuracy. Some of the differences between the three models are considerably larger than the standard errors. The fact that *ground truths* (LLRR and ALSEP locations) are only available for calibration on the near side also limits the potential accuracy of the models.

The histograms of the *x* and *y* components of the footprint residuals are strongly peaked, with most footprints located within 2 km of the model. The corresponding histogram for the *z* component is somewhat broader (Figure 5). The distribution of misclosures (a misclosure is defined as the deviation of Equation 3 from zero), normalized to the radius of the moon, is relatively fat-tailed because misclosures amalgamate the errors in all components. Yet radial errors still dominate the misclosures due to the lunar topography. Consequently, the *RMS* residuals cannot be effectively reduced to a level to reflect
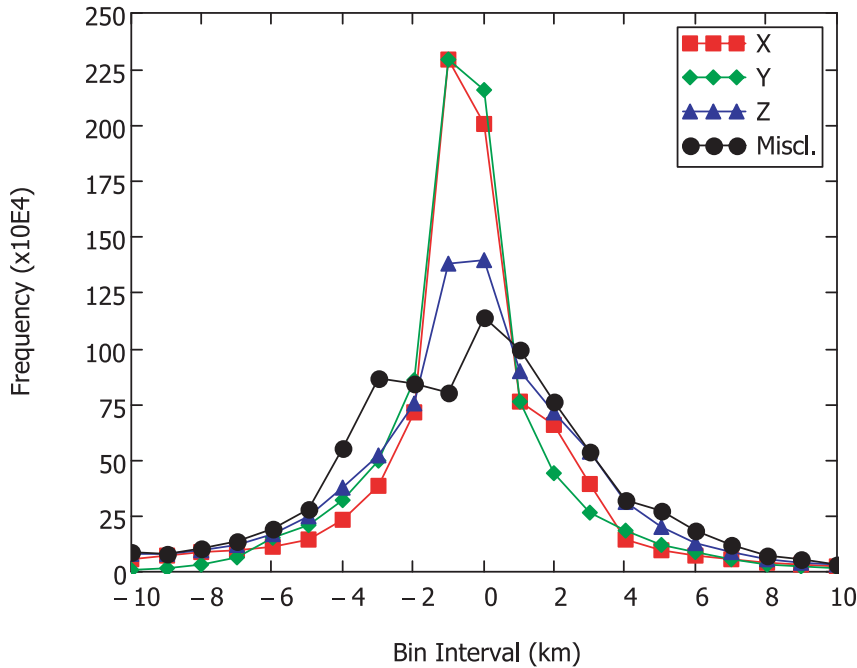
Figure 5: Histograms of the residuals for all footprints in the *Chang'E-1* dataset, separated into Cartesian components (XYZ). The model is the best-fitting biaxial ellipsoid. Misclosures are scaled to the average radius of the Moon.

the accuracy or precision of the solutions based solely on the observational errors in the coordinates because of the presence of the lunar topography in the radial values. For the new solutions presented here, the *RMS* residuals listed in Table 2 quantify the roughness of lunar topography as well as observational noise. That *Chang'E-1* data are noisier than the other data sets is also evident in the calibration results.

Given the small differences between their lunar figure parameters (Table 2), the triaxial and biaxial models cannot be differentiated. Nonetheless, as also discussed by Iz (2009), a biaxial ellipsoid is more appropriate for reasons of parsimony and for its conventional use in lunar mapping applications.

Comparison to spherical harmonic topographical models

Table 3 lists the lunar figure parameters derived from comparable spherical harmonic topographical models, namely the, CLTM-s01 model derived from an earlier dataset of 3 million *Chang'E-1* laser altimetry measurements (Ping et al. 2009), the STM 359_grid-02 model derived from 1.1 million *SELENE* laser altimetry measurements (Araki et al. 2009), and the *Clementine* GLTM-2 solution (Smith et al. 1997). The authors of these models did not publish realistic uncertainties and statistical details. It is also not evident whether the data were calibrated using LLRR and ALSEP locations.

Table 3: All units are meters. The first set of parameters in each row represents the *Chang'E-1* CLTM-s01 topographic model, calculated using 3 million footprints (Ping et al. 2009). The second set is the SELENE STM 359 grid-02 topographic model, based on 1.1 million footprints (Araki et al. 2009). The third set is the Clementine GLTM-2 solution (Smith et al. 1997). N/A: Not applicable. ?: Not reported.

Model	a	b	c	x_c	y_c	z_c	d_c	RMS
Biaxial	1737646 (?)	N/A	1735843 (?)	−1777 (?)	−730 (?)	237 (?)	1936	?
Ellipsoid	1738640 (?)		1735660 (?)	−1772 (?)	−731 (?)	239 (?)	1932	?
	1738139 (44)		1735972 (131)	−1740 (?)	−750 (?)	270 (?)	1914	?
Sphere	1737103 (?)	N/A	N/A	0	0	0	0	?
	1737150 (10)			0	0	0	0	?
	1737103 (10)			0	0	0	0	?

Other than the present paper, there is no published triaxial solution based on the recent laser altimetry measurements.

A comparison of the models summarized in Table 3 and Table 2 shows significant differences in the topographic and geometric solutions with respect to the lunar shape parameters. However, the coordinates of their geometric centers are in remarkably good agreement.

The biaxial equatorial and polar radii of the *Chang'E 1* and *SELENE* topographic models differ by −994 m[1] and 183 m respectively (subtracting their biaxial parameters). The geometric centers of these models agree remarkably well, to within a few meters. All biaxial shape parameters from the *Clementine* GLTM-2 solution, including the mean radii, differ considerably from the *Chang'E 1* and *SELENE* model estimates.

The discrepancies between the earlier topographical model based solutions and the geometric solutions reported in this study are due to the mathematical models and their solution approaches as well as the data. Although both spherical harmonic solutions and ellipsoidal solutions are algebraic in nature, meaning that the sum of the squared residuals can be minimized to find an optimal fit, the latter are more closely analogous to a traditional orthogonal distance fitting solution (Ahn et al. 2001) because the residuals really measure the distance of an altimeter measurement footprint from the model ellipsoid. Such solutions are known for their robustness (*ibid*). This is why the figure parameters and center derived from a harmonic topographic model are not equivalent to the geometric solutions.

In addition, the lunar shape parameters derived from a spherical harmonic topographic expansion are not optimal because the model contains a much larger number of parameters compared to the geometric 3D models used in this study. The lower number of degrees of freedom in the topographic solutions does not have a significant impact on the standard error of the estimated parameters, because the dataset is very large. However, a truncated harmonic series (omission error) may introduce systematic errors into the solutions. Ping et al. (2003) calculated that the truncation of a topographic model from the 180th degree and order down to the 140th degree and order resulted in RMS biases in the *Clementine*

Table 4: RMS misclosures of the spherical harmonic topographic models (listed in Table 3) and best fitting biaxial models (listed in Table 1). The dimensionless RMS misclosures are scaled by the average lunar radius in meters. [1]Spherical Harmonic Topographic Model, [2]Geometric Model, [3]Calibrated data.

Data\Model	Chang'E-1[1]	SELENE[1]	Chang'E-1[2]	SELENE[2]
Chang'E-1[3]	3931	4064	3196	4162
SELENE	4168	4528	3923	4143

laser altimetry data residuals close to 500 m. However, this error should be considerably less for the current harmonic models, which reach the 360th degree and order.

The RMS misclosures calculated for *Chang'E-1* and *SELENE* data using all estimated parameters (from topographic and geometric solutions) from equation (3), are listed in Table 4. These figures can be used to assess the overall goodness of fit of each solution. The models based on *SELENE* data all have larger RMS misclosures than models based on *Chang'E-1* data, despite the fact that the *Chang'E-1* data are noisier (Table 2). However, the RMS misclosure is also dependent on errors in the estimated model parameters. It is likely that the lunar figure parameters derived from the harmonic models are biased, because they are based on earlier, incomplete versions of the datasets. It is also likely that harmonic solutions are less influenced by variations in the lunar topography once the models are extended to a high degree and order.

Conclusion

Overall, the new lunar figure parameters reveal a more spherical shape, with an unprecedented precision down to the meter level. Yet there is still room for improvement, in particular regarding differences in the geometric centers of lunar figures estimated from *Chang'E-1* and *SELENE* data. For example, errors in the equatorial semi-major and polar axes of triaxial and biaxial lunar figures can be reduced by an improved analysis of satellite orbits. Such issues much be resolved before we can claim that the lunar figure is as accurate as it is precise.

Spherical harmonic models are powerful tools for the analysis of planetary topography. Nonetheless, the *Chang'E-1* lunar figure derived in this paper has

---

1 One of the reviewers remarked that the mean equatorial axis listed in Araki et al. (2009b) is a misprint. This difference becomes −257 m with the corrected mean equatorial radius.

a smaller RMS misclosure than previously published harmonic solutions. Note that geometric solutions perform equally well using either *Chang'E-1* or *SE-LENE* laser altimetry data.

Traditionally, the orientation of the best fitting geometric figure is not formulated for the sake of simplicity in mapping applications. The reference figures are implicitly constrained to ellipsoids whose axes are parallel to the underlying center of mass coordinate system, so these solutions do not reflect the true shape and orientation of the Moon. Smith et al. (1997) report significant tilting of the polar axis toward the Earth when the orientation of the lunar figure is accounted for in their solutions, and also derive different lunar shape parameters. If the usefulness of the best fitting lunar ellipsoid is to go beyond lunar mapping, then models must also take into account the orientation of the geometric figure. The *Chang'E-1* and *SELENE* laser altimetry datasets are detailed enough to take this step.

Acknowledgements

References

Ahn, J., W. Rauh and H. Warnecke, Least-squares orthogonal distances Fitting of circle, sphere, ellipse, hyperbola, and parabola, Pattern Recognition 34, pp. 2283–2303, (2001).

Araki, H., S. Tazawa, H. Noda1, Y. Ishihara, S. Goossens, S. Sasaki, N. Kawano, I. Kamiya, H. Otake, J. Oberst and C. K. Shum, Lunar Global Shape and Polar Topography Derived from Kaguya-LALT Laser Altimetry, Science Vol. 323, pp. 898–900, (2009a).

Araki, H., S. Tazawa1, H. Noda1, Y. Ishihara, S. Goossens, N. Kawano, S. Sasaki, I. Kamiya, H. Otake, J. Oberst and C. K. Shum, The Lunar Global Topography by the Laser Altimeter (LALT) Onboard Kaguya (SELENE): Results from the One Year Observation, 40th Lunar and Planetary Science Conference (2009b), www.lpi.usra.edu/meetings/lpsc2009/pdf/1432.pdf

Archinal, B. A., M. R. Rosiek, R. L. Kirk and B. L. Redding, The Unified Lunar Control Network 2005: U.S. Geological Survey Open-File Report 2006–1367 (2006). http://pubs.usgs.gov/of/2006/1367/

Bills, B. G. and A. J. Ferrari, A harmonic analysis of lunar topography, Icarus 31, 224–259 (1977).

Davies, M. E. and T. R. Colvin, Lunar coordinates in the regions of the Apollo landers, Journal of Geophysical Research, Vol 105 No. E8, pp. 20,277–20,280, (2000)

Gardner, C. S., Ranging Performance of Satellite Laser Altimeters; Proc. IEEE, Vol. 30, Issue 5, pp. 1061–1072, (1992).

Goossens, S., K. Matsumoto and H. Noda, 2009: Precise Orbit Determination of the Main Satellite of Kaguya, Presented at the 3rd KAGUYA(SELENE) Science Working Team Meeting, Tokyo.

İz, H. B., New Parameters of Geometrically Best Fitting Lunar Figures, Journal of Applied Geodesy, Vol. 3, pp 155–162 (2009).

İz, H. B., Y. Q. Chen, B. A. King, X. L. Ding and C. Wu, Deformation Analysis of the Unified Lunar Control Networks, Journal of Applied Geodesy, Vol. 3, pp 231–238 (2009).

JAXA, https://www.soac.selene.isas.jaxa.jp/archive/index.html.en (2009).

King, R. W., C. C. Counselman II and I. I. Shapiro, Lunar dynamics and selenodesy: Results from analysis of VLBI and laser data, J. Geophys Res., 81(35), 6251–6256, (1976).

Ping, J., Q. Huang, R. SHU and J. Yan, Lunar Topography Result from Chang'E-1 Laser Altimetry Mission, Presented at the 3rd KAGUYA(SELENE) Science Working Team Meeting, Tokyo, (2009).

Ping, J., Q. Huang, J. Yan, J. Chao, G. Tang and R. Shu, Lunar Topographic Model CLTM-s01 from Chang'E-1 Laser Altimeter Sc China Ser G-Phys Mech Astron vol. 52, 1105–1114 (2009).

Ping, J., K. Heki, K. Matsumoto and Y. Tamura, A Degree 180 Spherical Harmonic Model for the Lunar Topography, Adv. Space Res. Vol. 31, No. 11 pp 2377–2382, (2003).

Pope, A. J., Some Pitfalls to be Avoided in the Iterative Adjustment of Nonlinear problems, Proc. 38th an. meet. Am. Soc. Phot. (1972).

Ruben, L. J., An Analytical Study of Lunar Surface Shape and Size From Lunar Orbiter Mission I Photographs, NASA Technical Note-NASA JT D-5243 (1969).

Smith, D. E., M. T. Zuber, G. A. Neumann and F. G. Lemoine, "Topography of the Moon from the Clementine LIDAR," JGR, 102, no. E1, 1591–1611 (1997).

USGS Control Networks, http://astrogeology.usgs.gov/Projects/ControlNetworks/ (2008).

Author information

H. Bâki Iz and Y. Q. Chen
Dept. of Land Surveying and Geo-Informatics
The Hong Kong Polytechnic University
Hong Kong
E-mail: lshbiz@polyu.edu.hk

C. K. Shum and C. L. Dai
Division of Geodetic Science
School of Earth Sciences
The Ohio State University
USA